frontiers | Frontiers in Environmental Science

TYPE Original Research
PUBLISHED 19 November 2024
DOI 10.3389/fenvs.2024.1470746

OPEN ACCESS

EDITED BY
Chamindra L. Vithana,
Southern Cross University, Australia

REVIEWED BY
Jiachao Zhang,
Hunan Agricultural University, China
Guilherme Vanzetto,
Passo Fundo Educational Development Institute, Brazil

*CORRESPONDENCE
Shili Guo,
guoshili@swufe.edu.cn

RECEIVED 26 July 2024
ACCEPTED 05 November 2024
PUBLISHED 19 November 2024

CITATION
Li C, Xu W, Guo S, Shang S and Li BL (2024) Impact of gradient zero-valent iron pollution from steel works on soil microaggregate geochemical processes and dissipative structures.
Front. Environ. Sci. 12:1470746.
doi: 10.3389/fenvs.2024.1470746

Impact of gradient zero-valent iron pollution from steel works on soil microaggregate geochemical processes and dissipative structures

Chunjie Li[1,2,3], Wenbo Xu[4], Shili Guo[5]*, Songhao Shang[6] and B. Larry Li[7]

[1]School of Geographic Science and Tourism, Nanyang Normal University, Nanyang, China, [2]Key Laboratory of Natural Disaster and Remote Sensing of Henan Province, Nanyang Normal University, Nanyang, China, [3]Engineering Research Center of Environmental Laser Remote Sensing Technology and Application of Henan Province, Nanyang Normal University, Nanyang, China, [4]School of Resources and Environment, University of Electronic Science and Technology of China, Chengdu, Sichuan, China, [5]School of Economics, Southwestern University of Finance and Economics, Chengdu, China, [6]State Key Laboratory of Hydro science and Engineering, Department of Hydraulic Engineering, Tsinghua University, Beijing, China, [7]Department of Botany and Plant Sciences, University of California, Riverside, CA, United States

Abstract: Zero-valent iron (ZVI) contamination from steel works poses significant threats to soil quality and ecosystem health, particularly affecting soil microaggregates, which are fundamental to soil structure and function. In this study, we systematically investigated the impact of gradient ZVI pollution on the organic geochemical environment of soil microaggregates around steel works located in the core water source area of the Middle Route of the South-to-North Water Diversion Project in China. Advanced analytical techniques, including X-ray photoelectron spectroscopy (XPS), scanning electron microscopy (SEM), X-ray fluorescence spectroscopy (XRF), inductively coupled plasma optical emission spectroscopy (ICP-OES), X-ray diffraction (XRD), and Fourier transform infrared spectroscopy (FTIR), were employed to comprehensively characterize the geochemical processes, mineralogy, and organic matter environment of soil microaggregates. The findings revealed that soils near the steel works were acidified and strongly oxidized, with heavy metal contents, particularly Fe, significantly decreasing with increasing distance from the steel works (Fe content decreased from 27,516.2 mg/kg to 23,492.6 mg/kg). The pH of soils near the steel works was lower, while oxidation-reduction potential (ORP) and electrical conductivity were higher. XPS analysis indicated a higher content of reactive oxygen species (ROS) near the steel works and significantly lower soil organic matter content. The iron valence distribution showed spatial differences, with higher Fe^{2+} content on the surface of soil microaggregates near the steel works and Fe^{3+} dominating in areas farther away. These results suggest an evolutionary sequence of ZVI from Fe (0) oxidation to Fe(II) and then to Fe(III). The formation of dissipative structures in soil microaggregates due to ZVI contamination significantly affects soil physicochemical properties and the

organic environment. This study provides valuable insights into the multifaceted impacts of industrial activities on soil ecosystems and offers a scientific basis for soil conservation and remediation strategies.

KEYWORDS

zero-valent iron pollution, microaggregates, geochemical processes, organic matter dynamics, dissipative structure

1 Introduction

Soil, as a central component of the Earth's critical zones, exhibits extremely complex properties in its structure and functioning from nano-to macro-scale (Kuzyakov and Blagodatskaya, 2015). Soil microaggregates, as the basic units of soil structure, play a key role in numerous ecosystem processes, such as hydrological processes, soil erosion, microbial dynamics, and biogeochemical cycling (Cerdà, 1996; Kong et al., 2011; Lehmann and Kleber, 2015). However, the rapid development of the iron and steel industry in recent years has led to the release of large quantities of potentially toxic elements (PTEs), especially zero-valent iron (ZVI) pollution (Zhou et al., 2019). The latter has an active chemistry that serves as a superior electron donor and poses a severe threat to both soil quality and ecosystem health (dos Santos et al., 2022). The ZVI-based contamination seriously affects the quality of the surrounding soil, leading to the introduction of heavy metals and their compounds into the environment. As a result, the soil ecosystems are destructed and the environmental quality deteriorates. Iron minerals in ZVI-contaminated soils show a variety of chemical states, and the redox processes between Fe^{3+} and Fe^{2+} control iron transformation and bioavailability. Hence, the physicochemical properties, structural functions, geochemical processes, and mineralogy of soil microaggregates are significantly affected (Kögel-Knabner et al., 2010). Meanwhile, ZVI-based pollution considerably affects the formation and stability of soil microaggregates, which may lead to the destruction and dissolution of soil microaggregates. Consequently, soil ecosystem health is negatively affected (Marcon et al., 2021). The interaction of ZVI with dissolved organic matter (DOM) may also affect its reactivity to target pollutants. Thus, the chemical composition and stability of DOM could be altered, which in turn affects the local carbon cycle (Wang et al., 2020).

The Middle Route of the South-to-North Water Diversion Project in China's water source area is ecologically fragile. To this end, the changes and pollution problems in its surrounding environment may affect the water quality safety and water supply safety of the drinking water source area, which is a critical zone of the earth's surface with a fragile environment (Li and Guo, 2022; Sun et al., 2023). The previously reported works in the literature on ZVI are mostly found in laboratory studies (Bae and Lee, 2010). However, *in-situ* observational studies examining the impact of ZVI-based contamination on soil microaggregate geochemical processes in typical industrial zones in the region are still lacking. Industrial activities, especially steel production, are posing a serious threat to soil microaggregates. We hypothesize that: 1) the degree of ZVI-based pollution is negatively correlated with the distance from steel works; 2) ZVI-based pollution leads to gradient changes in the physicochemical properties of soil microaggregates and in the chemical environment of soil organic matter (SOM); and 3) ZVI-based pollution leads to the formation of dissipative structures in soil microaggregates. To test these hypotheses, we systematically sampled soils at varying distances from the steel works and employed advanced analytical techniques to analyze the physicochemical properties, mineralogy, and organic matter composition of soil microaggregates. In this work, the Middle Route of the South-to-North Water Diversion Project in China was selected as the study area around the steel works in the core water source area, and sample plots with different pollution gradients were selected. The goal was to systematically investigate the impact of the ZVI pollution gradient on the physicochemical properties of soil microaggregates and the chemical environment of organic matter (SOM). More specifically, it was examined: 1) how the ZVI-based pollution gradient affects the physicochemical properties of soil microaggregates; 2) the impact of the ZVI-based pollution on the organic environment of soil microaggregates; and 3) whether the ZVI-based pollution leads to the formation of dissipative structures in soil microaggregates and their ecological footprints. The geochemical processes, mineralogy, and organic matter composition of soil microaggregates were investigated by employing a variety of advanced analytical techniques, including XPS (to analyze surface elemental composition and chemical states), SEM (to observe soil microaggregate structure), XRF and ICP-OES (to determine elemental concentrations), XRD (to characterize mineralogy), and FTIR (to assess organic matter functional groups). These methods collectively enable a comprehensive understanding of how ZVI pollution affects soil microaggregate properties and processes. Our work provides an in-depth understanding of the impact of ZVI-based pollution on soil ecosystems. The transportation, transformation, and accumulation processes of the ZVI pollutants from the iron and steel industry in soils were elucidated. At the same time, the behaviour of biogeochemical processes at the micro level was explored. A scientific basis for the development of effective soil protection and remediation strategies is delivered in this work, which can be used as an important reference value for the protection of ecological and environmental safety of important water sources.

2 Materials and methods

2.1 Overview of the study area

This study area is located in the critical zone of the earth's surface of The Middle Route of the South-to-North Water Diversion Project in China. In particular, it is positioned in the hinterland of

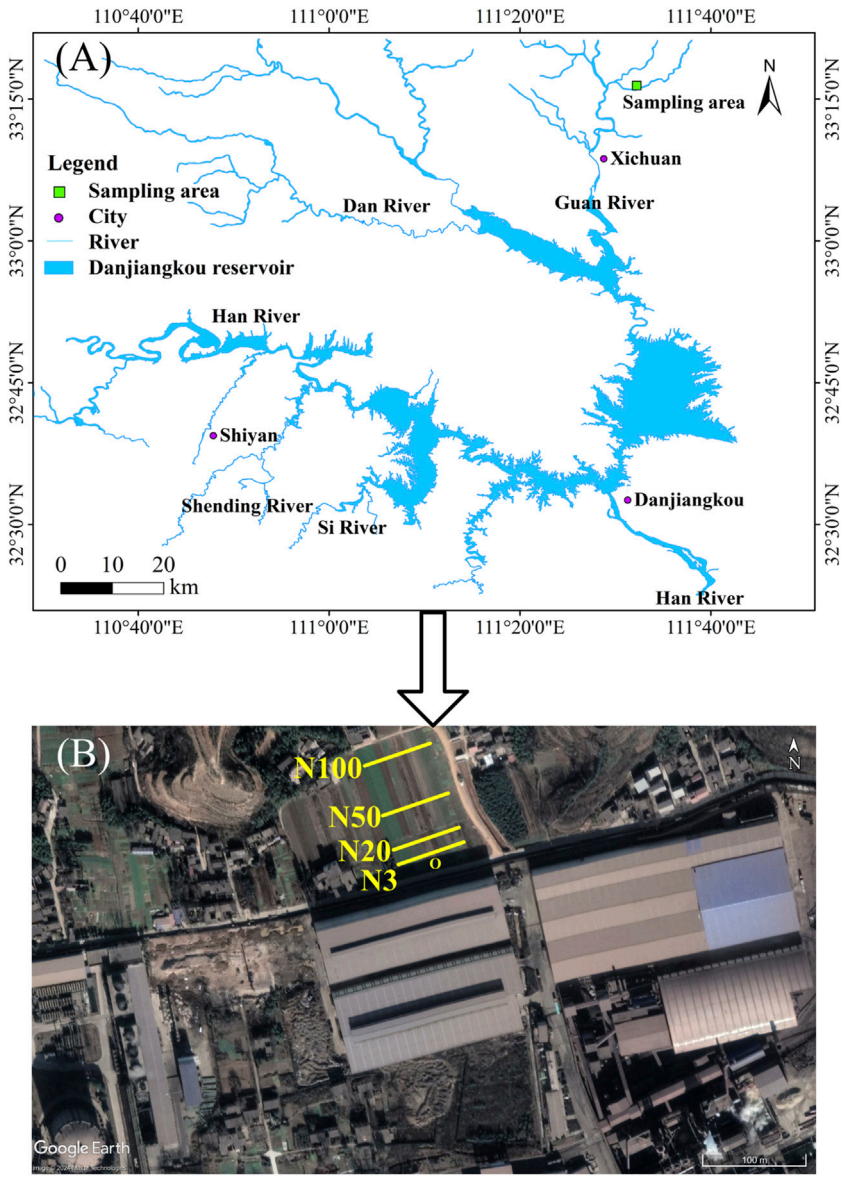

FIGURE 1
Map **(A)** shows the location of study area, and satellite photograph **(B)** shows the sampling sites of N3, N20, N50 and N100.

the core water source area, located in the transition zone between the northern subtropical and the warm temperate zones, and also the north-south transition zone of China's climate (Li et al., 2023). The Middle Route of the South-to-North Water Diversion Project in China is considered one of the largest trans-regional artificial water transfer projects in the world. Moreover, Danjiangkou Reservoir is the core water source area of the Middle Route of the South-to-North Water Diversion Project in China (Li et al., 2023), and is also an important drinking water source area supplying northern China (Li et al., 2015). The area is located in the northern subtropical monsoon climate zone and is significantly affected by the westerly wind belt, with an average annual temperature of 15.8°C and an average annual precipitation between 900 and 1,100 mm. The study sampling site is placed around Nanyang Hanye Special Steel Co., Ltd. (Figure 1). The company was established in 2003, a period that coincided with China's rapid growth in property, infrastructure development, and manufacturing from 2000–2020. The company's raw materials mainly came from the recycling of scrap iron and steel from building demolition, as well as factory end-of-life equipment. During this period, a large amount of scrap iron and steel was conveyed to the steel works for processing and treatment. In addition, one of the important processes was the crushing and milling of scrap iron. During the scrap iron crushing, milling, and smelting processes, a large number of micron-nanometre scale ZVI particles are released into the air. Subsequently, they are diffused through the atmosphere and settle in the surrounding area. Through naked eye observation and optical microscope examination, a large number of particles with reflective features, homologous to ZVI in the steel works, can be clearly seen in the soil. This phenomenon strongly confirms that the main pollutant in this area is ZVI. This pollution characteristic is closely related to the activities of the local steel industry, which provides an ideal research

scenario for studying the impact of ZVI from the steel industry on the surrounding soil environment. The choice of this area as a study object is of double significance: on the one hand, it shows the typical ZVI-based pollution characteristics of industrial zones. Due to its location at the Middle Route of the South-to-North Water Diversion Project in China's water source area, the results of the study not only help to understand the environmental behaviours of iron and steel industry pollutants, but also provide an important reference to protect the ecological and environmental safety of the water source areas. This study is a typical example of *in-situ* field research on the environmental impact of ZVI on soil's organic geochemical properties. Our work provides an important scientific basis for assessing the impact of industrial activities on the surrounding environment of the water source area and formulating the corresponding environmental protection strategies.

2.2 Collection and processing of soil samples

The sampling work in this work was carried out in August 2022, when Nanyang Hanye Special Steel Co., Ltd. has been in formal operation for 20 years. A systematic sampling programme based on a distance gradient was designed to comprehensively assess the soil contamination status of the area. Four parallel sampling strips, labelled N3, N20, N50, and N100, were set up around the steel works (Figure 1B). In this work, the gradient sampling strips were designed based on the discrete-phase model (DPM) dust particle dispersion model for the deployment of sampling points. The edge of the road in the steel works was defined as the starting point O (geographic coordinates: 33°16′25.39″N, 111°32′13.70″E; elevation: 236 m), and four sampling strips were located at 3, 20, 50, and 100 m from the starting point, respectively. The design of the gradient was intended to provide full coverage of the near strong, medium, and far weak pollution zones to accurately observe the gradient effect of the ZVI-based pollution. Each sampling strip was 50 m long and the samples were collected at 10 m intervals for a total of six samples. The focus was on collecting undisturbed soil samples from 0 to 20 cm depth to ensure that the samples were representative of the surface soil properties. Prior to sampling, dead leaves and branches were carefully removed from the surface to ensure the purity of the samples. Sample soils were thoroughly mixed and 500 g were randomly selected and brought back to the laboratory for analysis. To maintain the original state of the samples to the greatest extent possible, a well-designed treatment process was used: first, the samples were placed in a refrigerator at −80°C for 1 h, and then transferred to a freeze-dryer for low-temperature vacuum drying (parameters: vacuum degree 0.05 MPa, temperature −50°C, duration 24 h). The dried samples were carefully screened to remove large impurities, plant roots, and dead leaves. After initial sieving with a 2 mm mesh to remove coarse particulate matter, soil microaggregates were obtained by further sieving through a 0.25 mm mesh sieve to collect particles smaller than 0.25 mm, representing the microaggregate fraction. This approach ensured homogeneity and representativeness of the samples for subsequent analyses. This systematic sampling and processing method not only accurately reflects the gradient of the impact of the steel works pollution on the surrounding soil, but also ensures the quality and comparability of the samples. This approach lays a solid scientific foundation for subsequent detailed analyses.

2.3 Separation and extraction of soil microaggregates and SEM analysis

The experimental samples were mixed with 10 mol/L $Na_4P_2O_7$ for ultrasonication for 5 min. Then, 0.5 mol/L NaOH solution was added, and the reaction was carried out at 90°C for 30 min. Centrifugation was used to separate the solid phase from the liquid phase. The solid phase was washed with deionised water until neutral. The solid phase was then re-extracted with 0.5 mol/L HCl solution, and the extract was mixed with the washing solution. After that, ion exchange resin treatment was performed to remove impurity ions. Finally, the solid phase samples were washed to neutrality with deionised water. These chemical treatment steps were designed to maximise the separation and maintain the original structure of the soil microaggregates. SEM microscopy was used in the study to investigate the soil microaggregate structure (Zeiss GeminiSEM 360, ZEISS, Germany). Soil microaggregate powders were adhered to conductive adhesive during the experimental procedure and tested after gold spraying using an ion sputtering apparatus (Ersoy et al., 2008).

2.4 Methods for the determination of soil physical and chemical indicators

Soil temperature, humidity, and salinity were measured by TDR-310H (TDR-310H, produced by Acclima Company). Soil organic matter was measured by the scorching method, placing the samples in a muffle furnace at a scorching temperature of 650°C for 12 h. The difference between the weights before and after the scorching was weighed on an analytical balance as the weight of the organic matter, and averaged over three measurements for each sample. The weight was measured using an analytical balance (ME204/02, Mettler Toledo Company, Greifensee, Switzerland; measurement accuracy 0.0001 g). Soil pH was determined by utilizing a pH meter (PHS-25, Inesa-rex, China), and soil ORP was determined by using an ORP meter (TR-901, Inesa-rex, China).

2.5 Mineralogy analysis of soil microaggregates

XRD analysis was used to characterise the mineralogy composition of microaggregates in soil samples. SOC was removed with H_2O_2 (30%, analytically pure) in the pre-treatment to disperse the soil particles. Then, the samples were dried and ground with an agate mortar until they were free of particles. Finally, the samples were collected through a 400 mesh sieve. The mineral composition was analysed by conducting XRD measurements. The processed samples were made into powder wafers. The XRD analysis was carried out using an X-ray diffractometer (Rigaku smartlab9 automatic X-ray diffractometer). The following measurement conditions were used: Cu-Kα target; graphite monochromator filter; tube voltage: 40 kV; current: 150 mA;

scanning range: 5°–80° (2θ); scanning speed: 6°min-1 (2θ), step size 0.02°. The diffraction peaks obtained from the X-ray diffraction analysis were processed by the Jade software package. The results of the diffraction peaks were compared with the standard PDF cards to identify the type of clay minerals according to the clay mineral analysis method. Hence, the results of the physical phase analysis were obtained. According to the adiabatic method, the integrated intensities of selected diffraction peaks of clay minerals and various non-clay minerals on the diffraction pattern were measured, and the total clay mineral and non-clay mineral contents were calculated directly with the following formula:

$$X_i = \left[\frac{I_i}{K_i} \Big/ \left(\sum \frac{I_i}{K_i} \right) \right] \times 100\%$$

where X_i is the percentage content of i mineral in the sample, expressed as a percentage; K_i denotes the reference intensity of i mineral; I_i refers to the intensity of a diffraction peak of i mineral.

2.6 XRF and ICP-OES analyses

The dried soil samples were ground to 200 mesh, weighed, and pressed into thin slices. The samples were then placed in an X-ray fluorescence spectrometer for elemental analysis. The XRF analysis was performed using an AXIOS (PW4400) wavelength dispersive X-ray fluorescence spectrometer (PANalytical B.V., Almelo, the Netherlands). It has a maximum power of 4.0 kW, a maximum excitation voltage of 60 kV, a maximum current of 125 mA, an super sharp tube ceramic end window (75 μm), an Rh-targeted X-ray tube, and a 68-position (32-mm diameter) sample changer. The SuperQ 4.0 quantitative analysis software was used, from which spectral line intensity calculations, Compton scatter-ray internal standard correction, interference spectral line correction, and matrix correction were performed automatically, and the results were displayed. At the same time, the information on MgO, P_2O_5, K_2O, and CaO content was obtained by performing XRF quantitative analysis. The ICP-OES analysis was performed by Agilent Technologies 5110 ICP-OES. Instrument parameters: argon supply pressure of 0.650 MPa; sample injection pump speed: 80 r/min; instrument cleaning pump speed: 60 r/min; sample injection delay: 20 s; sample injection stabilisation time: 10 s; Integration time: 5 s; RF power 1,200 W; nebuliser flow: 0.60 L/min; observation mode is axial.

2.7 XPS analysis

XPS is a surface-sensitive chemical analysis technique that measures the electronic states of elements on the surface of materials and is widely used in soil environmental analysis. With a sampling depth of 2–5 nm, XPS is capable of identifying and analysing changes and distributions of organic functional groups and iron oxides on the surface of soil microaggregates. Significant spatial differences in soil surface elemental composition and chemical state with distance from steel works can be also characterised (Yao et al., 2010; Huang et al., 2017). This technique helps to understand the distribution of soil organic matter, the mechanism of metal oxide formation, and the migration law of heavy metal pollution. The interaction between organic matter and soil microstructure can be studied, which provides a powerful tool for solving soil environmental problems. The principle of XPS is to use a focused X-ray beam to excite electrons on the surface of the sample, and then collect and analyse the resulting photoelectrons to determine the chemical composition of the sample and its relative proportions. The XPS analysis was performed using a Thermo Scientific Nexsa, where the vacuum of the analysis chamber was 8×10^{-10} Pa, the excitation source was Al ka rays (hv = 1,486.6 eV), the operating voltage was 12.5 kV, the filament current was 16 mA, and the signal accumulation was performed for 10 cycles. Passing-Energy was tested with a full spectrum of 100 eV, a narrow spectrum of 30 eV, a step size of 0.1 eV, a dwell time of 40–50 ms, and a charge correction using C1 s = 284.80 eV binding energy as the energy standard. Data analysis and processing were undertaken using the XPSPEAK Version 4.1 software package. The data processing steps of XPSPEAK Version 4.1 software mainly include: background deduction, energy correction, setting fitting parameters and constraints, and iterative fitting. The relative content of each phase was calculated by fitting the peak area and calculating the ratio of the peak area to the total area.

2.8 FTIR analysis

The rapid development of FTIR has provided an efficient means of characterising the molecular compositional structure and features of soil SOM, as can be ascertained by a number of works in the literature (Margenot et al., 2015). The FTIR method has significant advantages in characterising the soil organic environment. The analysis process started with separate random samples of sieved naturally air-dried soil samples, picking out stones, and roots and passing them through a 0.149 mm soil sieve. The samples were then mixed with dried potassium bromide (spectroscopically pure) at a mass ratio of 1:90 and ground manually in an onyx mortar under an infrared lamp for rapid and thorough grinding. It was compacted with a tablet press at 10 kPa and placed in a Thermo Nicolet iS5 Fourier transform infrared spectrometer (ThermoFisher Scientific, United States) to be measured (Li et al., 2022). KBr was used as the background value, and the spectra were collected in the range of 400–4,000 cm^{-1} with a resolution of 4 cm^{-1} and a scanning frequency of 32 times. Each sample was repeated five times, and the average value was taken after a similarity comparison. The background value was deducted to obtain the infrared spectra of the samples. The raw spectral data were corrected using the correction function of the Thermo Scientific OMNIC software 6.0 package to remove the baseline effect and then normalised to the standard. Finally, the software was used to calculate the integral of the relative peak area of the main peak.

2.9 Data statistics and graphing

Statistical analyses were performed using SPSS 15.0 for Windows (SPSS Inc., Chicago, IL). The map was generated using ArcGIS 10.0 (ESRI, Redlands, CA, United States: http://www.esri.

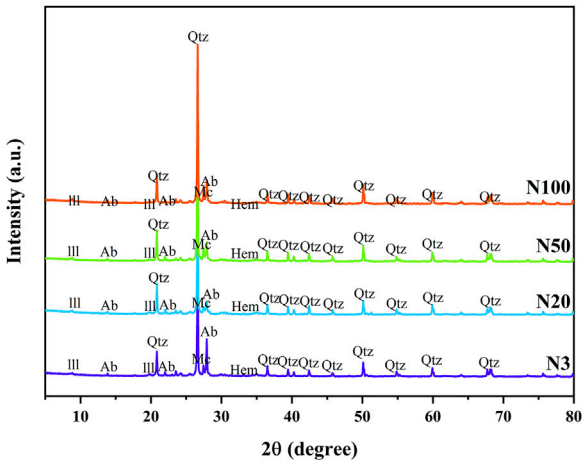

FIGURE 2
X-raydiffractogram patterns (Cu-Kα radiation) and mineral change at different sampling locations (Ill, illite; Mc, microcline; Ab, albite; Hem, hematite; Qtz, quartz).

com/software/arcgis). All bar charts, pie charts, and spectrograms were generated using the Origin 8.1 software package (Origin Lab Corp. v 8.1). Satellite images in Fig. 1(II) were obtained from Google Earth Pro (free version, Google Earth).

3 Result and analysis

3.1 Soil microaggregate mineralogy and geochemical characteristics

The results of soil mineralogy analyses revealed the spatial variability pattern of soil mineralogy properties around the steel works. The XRD analyses showed that the soils in the study area were mainly composed of Illite, Microcline, Albite, Quartz, and a small amount of Hematite (Figure 2; Table 1). Quartz, as the most dominant mineral fraction, exceeded 48% in all sample sites. The Illite content showed a clear decreasing trend from 18.0% ± 0.8% at location N3 near the steel works to 12.7% ± 0.6% at the farthest location N100. On the contrary, the Microcline content increased at a distance from 9.1% ± 0.5% at N3 to 15.0% ± 0.5% at N100. The Albite content was more complex, being highest at N3 (23.2% ± 0.5%), then sharply decreasing to 16.1% ± 0.3% at N20, before recovering slightly at N50 and N100. The Hematite content was lower and less variable, being slightly higher at position N3 (1.5% ± 0.2%) and remaining between 1.0% and 1.2% at other positions (Table 1). These patterns of mineralogy change reflect the impact of steel works activities on the mineralogy of the surrounding soils. The Microcline content increased while the Illite content decreased with increasing distance from the steel works. Illite is often regarded as a secondary mineral and the increasing amount of illite may reflect the phenomenon of evolution of primary and secondary minerals. The small changes in the hematite content may be related to the input and transformation process of ZVI. These findings provide an important basis for deeply understanding the impact of industrial activities on soil mineralogy properties. They also highlight the complexity of the spatial distribution of soil mineralogy and deliver a new perspective for further research on the impact of iron and steel industrial activities on soil ecosystems.

TABLE 1 Mass fraction of soil mineral using XRD with standard deviation at different sampling locations (%).

Mineral	N3	N20	N50	N100
Illite	18.0 ± 0.8	16.9 ± 0.6	15.4 ± 0.6	12.7 ± 0.6
Microcline	9.1 ± 0.5	12.0 ± 0.4	13.4 ± 0.4	15.0 ± 0.5
Hematite	1.5 ± 0.2	1.1 ± 0.1	1.0 ± 0.2	1.2 ± 0.2
Albite	23.2 ± 0.5	16.1 ± 0.3	17.7 ± 0.4	18.9 ± 0.4
Quartz	48.2 ± 0.6	53.8 ± 0.5	52.5 ± 0.5	52.2 ± 0.5

The results of the study showed that the N3 sample had the lowest pH value of 4.45 while the N100 sample had the highest pH value of 5.66 (Table 2). This outcome indicates that soil pH varies at different locations. The highest redox potential (ORP) of 366.00 mV was recorded for the N20 sample, while the lowest ORP of 346.33 mV was recorded for the N100 sample. Thus, it can be argued that the soil has higher oxidation status in the location close to the steel works. This result points out that the soil redox condition also varies in different locations. Sample N3 exhibited the highest conductivity of 230.50 uS/cm while sample N100 had the lowest conductivity of 129.14 uS/cm. This result suggests that soil salinity also varies at different locations. The SOM contents were all in the range of 2%–4% indicating that the SOM contents were similar at different locations. However, the N100 sample had the highest and the N3 sample had the lowest (Table 3). As the distance from the steel works increased, the pH and organic carbon content showed an increasing trend, while the ORP and conductivity displayed a decreasing trend. The highest MgO content was found in the N20 sample, and the highest contents of P_2O_5, K_2O, and CaO were found at the N100 position, of which K_2O and CaO were alkaline compounds. The higher pH value at N100 is more favourable for alkaline compounds (Table 2; Table 3). Heavy metals were analysed by using two analytical methods, namely, ICP-OES and XRF, to determine the contents of various elements (As, Cr, Cd, Cu, Fe, Mn, Ni, Pb, Se, Zn, Ti, Rb, Sr, Y, Zr, Ag, Ba) in samples collected from different locations (N3, N20, N50, N100) (Table 4). The content of different elements in the soil had different trends with increasing distance from the steel works: the content of Fe significantly decreased from 27,516.2 mg/kg to 23,492.6 mg/kg, indicating that the concentration of Fe decreased with increasing distance (Table 4). The content of Mn slightly decreased from 300.4 mg/kg to 283.4 mg/kg. The content of Cr decreased from 35.4 mg/kg to 28.7 mg/kg showing a decreasing trend. The content of Zn showed an increasing and then decreasing trend, reaching a peak of 71.9 mg/kg at 20 m from the steel plant, followed by a gradual decrease at 50 and 100 m (Zhou et al., 2019). The content of Ti also showed a decreasing trend from 3,208 ± 53 mg/kg to 2,837 ± 49 mg/kg. The content of As decreased from 12.5 mg/kg at N3 to 7.0 mg/kg at N100, indicating that the content of As decreases with the increase of the distance (Zhou et al., 2019). Mn, Cr, Zn, Ti, and As showed a similar distribution pattern as Fe, and these elements are

TABLE 2 Physicochemical properties of soil at different sampling locations.

Sampling locations	PH	ORP (mv)	Conductivity (us/cm)	Temperature (°C)	Soil moisture (%)
N3	4.45	364.50	230.50	22.55	26.40
N20	4.62	366.00	229.75	22.35	25.25
N50	5.22	355.67	216.33	22.50	28.10
N100	5.66	346.33	129.14	23.40	27.99

TABLE 3 Soil organic matter and nutrient content at different sampling locations.

Sampling locations	SOM(%)	MgO (g/Kg)	P_2O_5 (g/Kg)	K_2O (g/Kg)	CaO (g/Kg)
N3	2.70	3.28 ± 1.37	0.18 ± 0.02	1.67 ± 0.02	0.73 ± 0.01
N20	2.80	4.20 ± 1.42	0.22 ± 0.02	1.79 ± 0.02	0.71 ± 0.01
N50	3.20	3.72 ± 1.55	0.20 ± 0.02	1.76 ± 0.02	0.79 ± 0.01
N100	3.70	3.26 ± 13.13	0.29 ± 0.02	1.92 ± 0.02	0.87 ± 0.01

TABLE 4 Mass fraction of soil heavy elements using ICP-OES and XRF with standard deviation (mg/kg).

Heavy elements	Methods	N3	N20	N50	N100
As	ICP-OES	12.5	11.6	7.3	7.0
Cr	ICP-OES	35.4	33.8	30.8	28.7
Cd	ICP-OES	<5.0	<5.0	<5.0	<5.0
Cu	ICP-OES	16.3	<5.0	<5.0	<5.0
Fe	ICP-OES	27,516.2	26,015.1	24,845.9	23,492.6
Mn	ICP-OES	300.4	290.4	287.6	283.4
Ni	ICP-OES	15.7	22.7	23.6	22.9
Pb	ICP-OES	<5.0	<5.0	<5.0	<5.0
Se	ICP-OES	<5.0	<5.0	<5.0	<5.0
Zn	ICP-OES	65.1	71.9	67.6	64.7
Ti	XRF	3,208 ± 53	3,169 ± 51	3,234 ± 57	2,837 ± 49
Rb	XRF	102 ± 16	93 ± 15	97 ± 15	98 ± 15
Sr	XRF	191 ± 20	177 ± 18	192 ± 19	219 ± 20
Y	XRF	30 ± 18	23 ± 16	31 ± 17	27 ± 17
Zr	XRF	196 ± 17	182 ± 15	172 ± 15	166 ± 15
Ag	XRF	44 ± 32	49 ± 31	35 ± 31	41 ± 31
Ba	XRF	438 ± 365	481 ± 352	437 ± 354	500 ± 353

common elements in steel works in the steelmaking process. The trend of the content of other elements (e.g., Rb, Sr, Y, Zr, Ag, and Ba) with distance is more complicated. Some elements, such as Sr and Ba, were more abundant at N100 than at other locations, which may be related to natural distribution and transport in the soil. The contents of Cd, Pb and Se elements exceeded the sensitivity limit of the instrument.

3.2 Analysis of the surface organic environment and chemical state of soil microaggregates

The chemical state analysis of carbon showed that C-C/C=C was the most dominant chemical state, with the highest percentage at the N100 position. This effect may imply that areas further away from

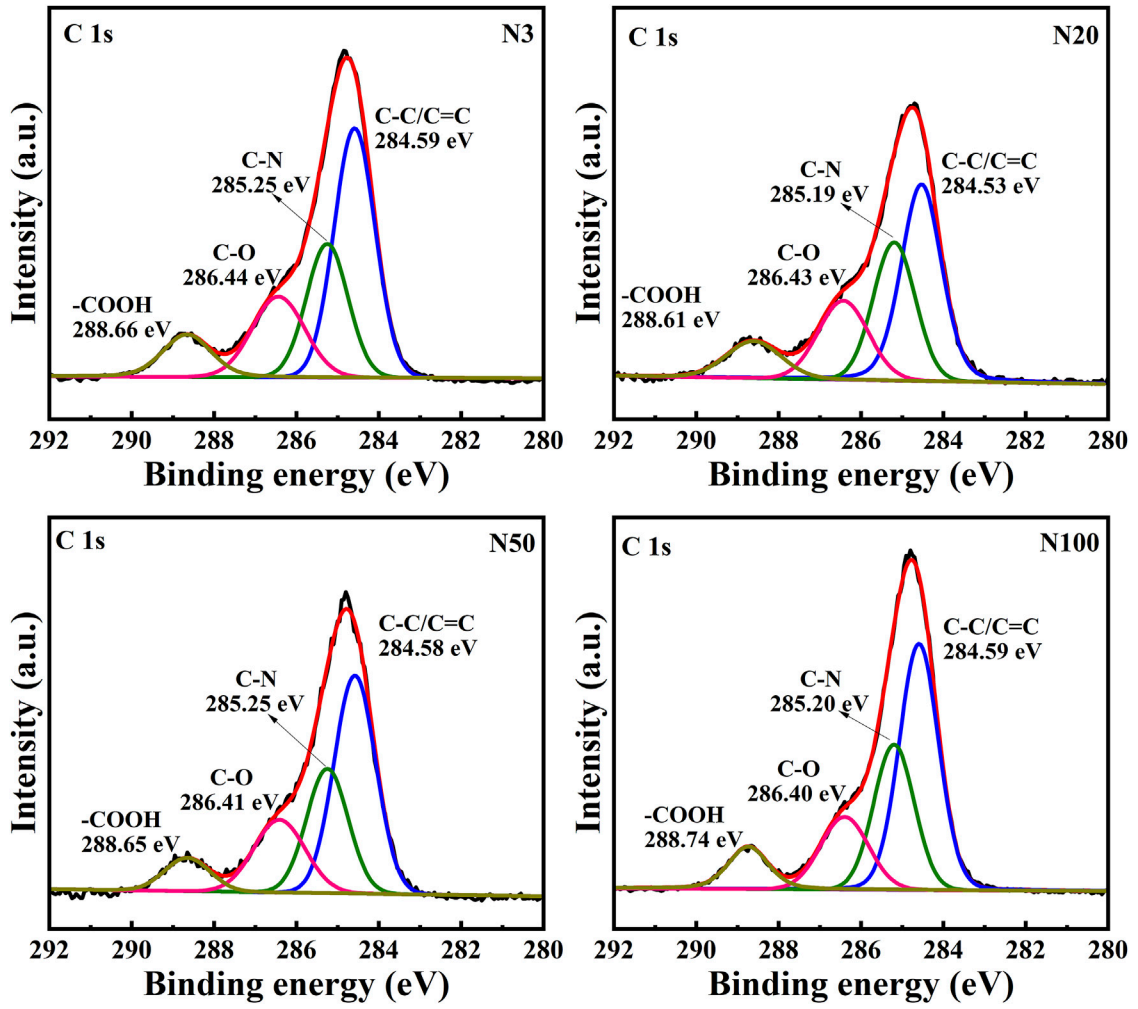

FIGURE 3
The XPS spectra of C 1 s and curve resolution into different components.

the steel works retained more of the original organic matter structure (Figure 3; Table 5). C-N, as the second major chemical state of carbon, had the highest percentage at the N20 position, suggesting that a high level of nitrogenous organic matter may be present in this area. C-O was the third major chemical state of carbon, with the highest proportion at N20 (Figure 3). This distribution trend may be related to the degree of oxidation of soil organic matter, which may be higher near the steel works. COOH was the least significant carbon chemical state. Nonetheless, it still reached the highest value at N20. This outcome further confirms that the area close to the steel works may have experienced a more intense oxidation of organic matter. The presence of C-O and Si-O confirms the presence of carbon oxides and silicon oxides in the samples, which may be related to soil mineralogy (Huang et al., 2017) (Figure 4; Table 5). From N3 to N100 distance, a trend of gradually increasing content of C-C/C=C was detected (Huang et al., 2017), while the content of C-O and COOH relatively decreased (Yao et al., 2010). This trend may reflect the gradual ageing and oxidation of organic matter in proximity to steel works. C-C/C=C may represent fresher organic matter, while C-O and COOH may be aged organic matter that has undergone oxidation and acid digestion reactions. The chemical state distribution of nitrogen also showed significant spatial differences. The Pyridinic-N content was highest at the N100 position with 45.33% (Kelemen et al., 2002); The Pyrrolic-N content reached its maximum at N50 with 31.98% (Zhu et al., 2016). The Quaternary-N content was highest at the N20 position with 30.50%, while Oxizided-N reached its maximum value of 25.85% at the N100 position (Figure 5; Table 5). These results point out that the chemical state of Nitrogen significantly changes with the distance from the steel works. The analysis of elemental calcium revealed that the binding energies of Ca 2p3/2 and Ca 2p1/2 were higher at locations closer to the steel works, implying that calcium is more susceptible to electron loss at locations close to the steel works. This effect may be related to the lower pH of the soil near the steel works (Table 2). Overall, the average percentage of Ca 2p1/2 was higher than that of Ca 2p3/2, with the highest percentage of Ca 2p3/2 at N100 and the highest percentage of Ca 2p1/2 at N20 (Figure 6; Table 5). This distribution may reflect the spatial variability of different forms of Ca compounds in the soil. Fe is present in both Fe^{2+} and Fe^{3+} valence states (Yamashita and Hayes, 2008). Figure 8 depicts the concentration and valence distribution of

10.3389/fenvs.2024.1470746

TABLE 5 XPS quantitative analysis of core levels and chemical states at different sampling locations.

Core levels	Chemical states	N3		N20		N50		N100	
		Peak position (eV)	%	Peak position (eV)	%	Peak position (eV)	%	Peak position (eV)	%
C 1s	C-C/C=C	284.59	45.88%	284.53	41.94%	284.58	46.64%	284.59	47.02%
	C-N	285.25	24.90%	285.19	28.39%	285.25	26.49%	285.2	27.49%
	C-O	286.44	19.08%	286.43	19.42%	286.41	19.13%	286.4	16.35%
	COOH	288.66	10.14%	288.61	10.25%	288.65	7.74%	288.74	9.15%
O 1s	Al_2O_3	531.27	21.13%	531.27	25.81%	531.30	28.23%	531.37	28.60%
	C-O	532.05	39.07%	532.08	40.13%	532.13	41.04%	532.12	37.79%
	Si-O	532.86	29.12%	532.87	22.43%	532.99	25.08%	532.94	23.79%
	COOH	533.71	10.69%	533.66	11.63%	533.96	5.65%	533.72	9.82%
N 1s	Pyridinc-N	399.36	37.60%	399.27	40.74%	399.19	31.37%	399.33	45.33%
	Pyrrolic-N	400.52	22.37%	400.17	28.77%	399.65	31.98%	399.92	28.82%
	Quaternary-N	401.99	19.48%	401.69	30.50%	400.73	14.08%	N/A	N/A
	Oxizided-N	403.11	20.55%	N/A	N/A	402.22	22.58%	399.33	25.85%
Ca 2p3/2	N/A	348.78	39.30%	348.95	32.35%	348.54	40.45%	348.47	40.47%
Ca 2p1/2	N/A	351.94	60.70%	352.09	67.65%	351.85	59.55%	351.68	59.53%
Fe 2p3/2	Fe^{2+}	712.30	28.04%	712.02	30.48%	712.44	31.45%	N/A	N/A
	Fe^{3+}	714.07	42.86%	713.51	32.22%	714.7	23.31%	713.24	53.32%
Fe 2p1/2	Fe^{2+}	724.23	16.50%	724.67	19.08%	725.59	23.44%	N/A	N/A
	Fe^{3+}	727.23	12.60%	727.42	18.22%	728.16	21.80%	726.17	46.68%

Fe at different sampling locations and the variation in the proportion of Fe_2O_3. The total Fe concentration showed a clear spatial gradient from about 27,516.2 mg/kg at N3 to about 23,492.6 mg/kg at N100, indicating that the Fe content in the soil gradually decreased with the increasing distance from the steel works. The valence distribution of Fe also presented significant spatial differences. At N3, N20, and N50 locations, Fe^{2+} and Fe^{3+} coexisted (Figures 7, 8; Table 5). However, at N100, all Fe was present in the Fe^{3+} chemical state, probably reflecting the significant changes in the redox environment of the soil with the increasing distance from the steel works. Although the proportion of Fe_2O_3 fluctuated among different sampling sites, the overall variation was not significant, with the highest at N3, the lowest at N50, and a slight increase at N100 (Figure 8). These observations not only reflect the differences in soil redox environments, but may also suggest an evolutionary sequence from Fe (0) oxidation to Fe(II) and eventually to Fe(III). In-laboratory controlled experiments also confirmed the occurrence of oxidation in nano-ZVI with an evolutionary sequence from Fe (0) oxidation to Fe(II) and then to Fe(III) (Bae and Lee, 2010; Bae and Hanna, 2015; He et al., 2016). This variation in the spatial distribution of Fe valence states may be related to differences in soil redox environments and may reflect the impact of steel works activities on the cycling of Fe in the surrounding soils. These findings not only reveal the complex spatial distribution of the elemental compositions and chemical states on the soil surface around the steel works, but also provide an important basis for deeply understanding the impact of the steel works activities on the surrounding soil environment. Such changes in the Fe chemical state may have important implications on soil microbial activities, organic matter stability, and geochemical processes, providing an important basis for understanding the impact of the ZVI-based pollution on soil Fe cycling.

3.3 Analysis of the molecular structure and functional groups of soil microaggregates

By analysing the molecular structure and functional groups of soil microaggregates, the peak at 3,637–3,645 cm^{-1} was detected, which can be assigned to the hydroxyl group stretching vibration absorption peak and corresponds to clay minerals (Nguyen et al., 1991; Peltre et al., 2014). The broad peak 3,436–3,445 cm^{-1} can be attired to the O-H stretching vibration of phenols and alcohols. The FTIR integration area was largest at position N3 in the wave number range 3,436–3,445 cm^{-1}, and decreased with the increasing distance from the steel works (Figure 9; Table 6). The peak at 1,649–1658 cm^{-1} can be assigned to the C=O vibrations in carboxylic acids/anions and amides, the C=C stretch in aromatics, and the O-H bending in mineral-water (Soriano-Disla et al., 2014) (Figure 9). In the wave number range 1,649–1,658 cm^{-1}, the FTIR integration area was largest at position N3 and smallest at

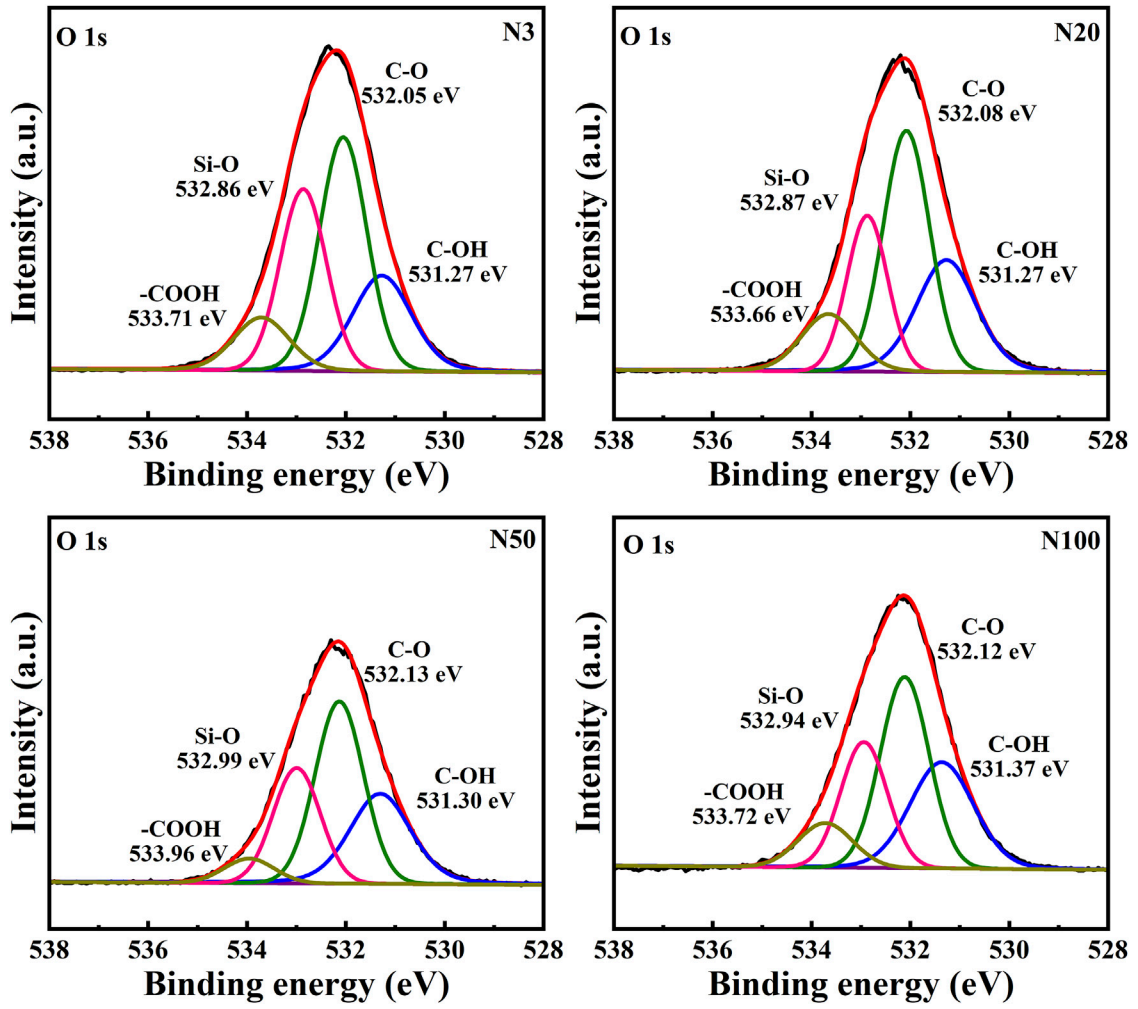

FIGURE 4
The XPS spectra of O 1 s and curve resolution into different components.

position N100. The absorption peaks near 1,038–1,050 cm^{-1} correspond to the stretching vibrations of the C-O stretching of polysaccharide or polysaccharide-like substances and also the absorption peaks of the stretching vibrations of Si-O. In the wave number range of 1,038–1,050 cm^{-1}, the FTIR integration area at the N3 position was the largest at 12.227 ± 0.666, and the smallest at the N50 position. The peak at 792–782 cm^{-1} originated from the NH_2 out of plane vibration of Primary amine or the peak of -CH out of plane bending vibration of aldehydes (Krivoshein et al., 2022). Additionally, and the N50 position had the largest FTIR integration area of 0.981 ± 0.034, while the other positions had relatively small FTIR integration areas. The peak near 469–472 cm^{-1} can be assigned to SiO2, originating from the O-Si-O bending (Krivoshein et al., 2022).

4 Results and discussion

4.1 Influence of the ZVI-based pollution gradient on biogeochemical processes of mineralogy elements in soil microaggregates

The significant impact of the ZVI-based pollution gradient on mineralogy and elemental geochemical processes in soils around steel works was presented here. From our analysis, it was demonstrated that the content of heavy elements (e.g., Fe, As, Cr, Cu, Mn, Zr) increased with proximity to the steel works (Table 4). This distribution pattern strongly suggests that steel works are the main source of these elements, highlighting the potential impact of industrial activities on the surrounding soil environment. Quantitative XRD analyses displayed a decreasing trend in illite content and an increasing trend in microcline content with the increasing distance from the steel works. This result suggests that the activities of the steel works may have affected the mineralogy of the surrounding soils, leading to an inverse change in the content of these two minerals. The XPS analyses revealed a complex valence distribution of Fe in the soil, mainly including Fe-oxide, Fe-hydroxide, Fe-suboxide, and organic Fe. In-laboratory controlled experimental studies showed that the main by-products generated

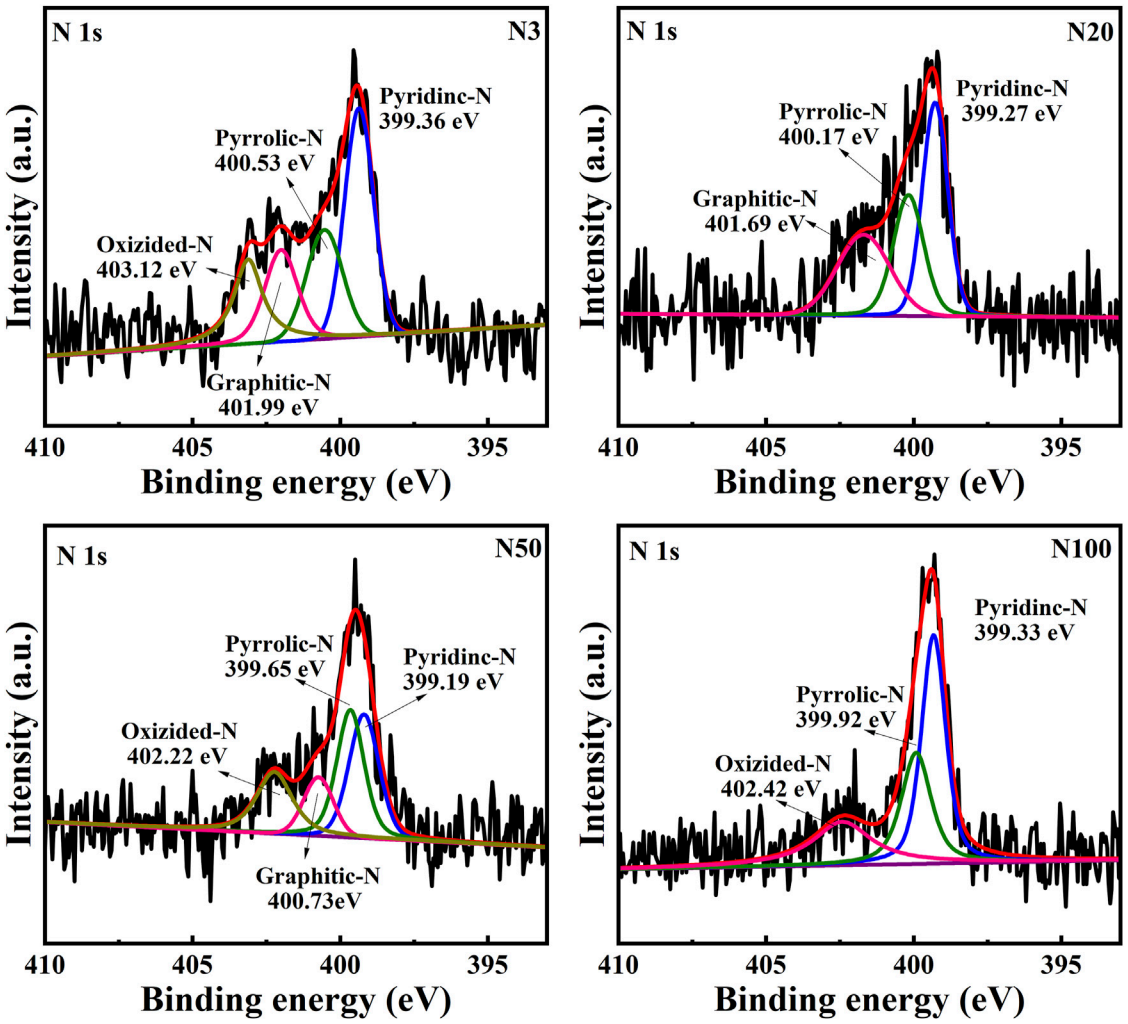

FIGURE 5
The XPS spectra of N 1 s and curve resolution into different components.

during nano-ZVI passivation including magnetite and acicular ferrite, were similar to the ZVI by-products observed in this work (Bae et al., 2018). Particularly noteworthy was the variation in the relative contents of Fe^{2+} and Fe^{3+} with distance indicating the spatial heterogeneity of the soil redox environment. The gradient effect of the ZVI-based pollution was further confirmed by the valence distribution of Fe. The relative content of F^{e2+} was higher at the N3, N20, and N50 locations, while at the N100 location the iron ions were all Fe^{3+} (Figures 7, 8; Table 5). Relevant experimental studies have shown that oxidation reactions occur in ZVI, with an evolutionary sequence from Fe (0) oxidation to Fe(II) and then to Fe(III) (Bae and Lee, 2010; Bae and Hanna, 2015; He et al., 2016). The severity of Fe toxicity is related to the oxidation state of Fe in the order Fe (0) > Fe(II) > Fe(III) (Auffan et al., 2008). N3 is highly biotoxic due to the high Fe (0) content and no obvious bacterial residues were observed in the SEM photographs. On the contrary, bacterial residues can be clearly observed at the N20 position, suggesting that the microbial activity is intense at this position (Figure 10). The variation of the Fe(II)/Fe(III) ratio affects soil microaggregates bioavailability. The heterogeneity in the valence distribution of Fe may originate from the direct impact of steel works emissions on the physico-chemical properties of the soil. This inference is further supported by the increase in pH with increasing distance and the decrease in ORP and conductivity observed in the study. Fe(III) can form stable complexes with organic matter and protect organic carbon from microbial degradation. Fe(II) may also disrupt this complex and accelerate the decomposition of organic matter (Zhang et al., 2014). In particular, the observed increase in the ORP values with proximity to the steel works suggests a more intense oxidative environment, which may promote the oxidation and fixation of certain metal elements. The Fe contamination gradient not only altered the basic physicochemical properties of the soil, but also significantly affected the structure formation, elemental distribution, and geochemical processes of soil microaggregates (Table 4; Figure 10). This distribution pattern not only reflects the existence of spatial differences in soil redox environments, but also hints at the critical role of iron cycling as an important pathway for surface material-energy flow in contaminant transport and transformation processes (Melton et al., 2014; Hu et al., 2018). The presence of ZVI may lead to lower phosphorus

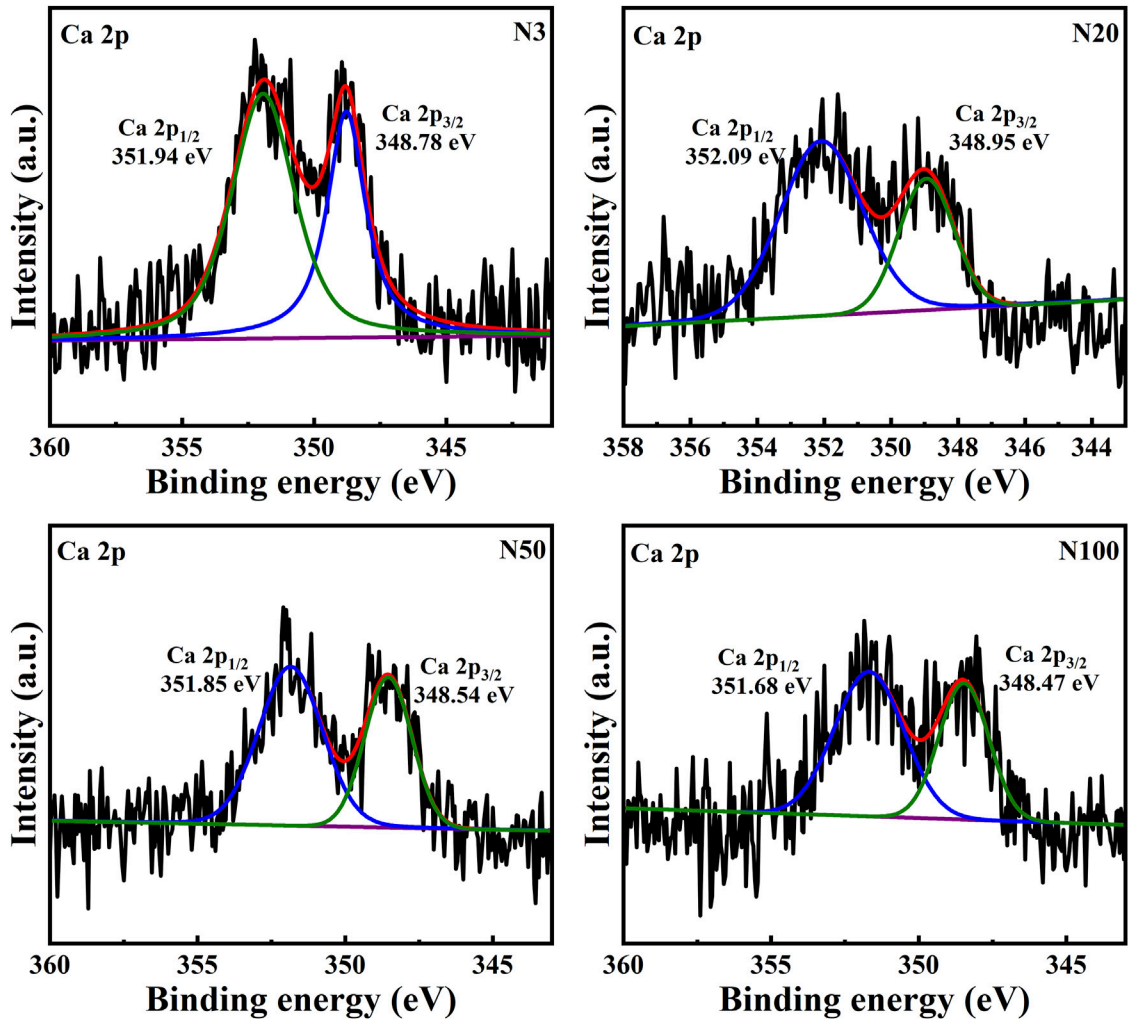

FIGURE 6
The XPS spectra of Ca 2p and curve resolution into different components.

content in the soil, which is consistent with the low P_2O_5 content observed in this study at the N3 location. The results of elemental Ca analyses, especially the change in the binding energy of Ca 2p3/2 and Ca 2p1/2, imply that calcium ions are more susceptible to electron loss in the near steel works. This effect may be related to the lower pH in the near steel works area, further confirming the influence of steel works emissions on the soil biogeochemical processes. Meanwhile, the relative deficiency of K_2O at the N3 location may be indicative of elemental loss phenomena, which may be related to soil acidification and ion exchange processes (Table 2).

4.2 Impact of different gradients of the ZVI-based pollution on the organic environment of soil microaggregates

In this work, the impact of the ZVI-based pollution on the soil microaggregate organic environment at different distances around steel works was investigated by using advanced analytical techniques, such as XPS and FTIR. The results revealed the significant influence of the ZVI-based pollution gradient on the composition, structure, and distribution of soil microaggregate organic matter, as well as a series of complex biogeochemical processes triggered by it. The XPS results helped to elucidate the differences in soil organic environment under the differences in the ZVI-based pollution gradient. The results of the XPS analyses showed the existence of significant differences in the chemical state of carbon at different sampling locations, reflecting the spatial heterogeneity of organic matter composition and structure ((Figures 3–5; Table 5). C-C/C=C, as the most dominant chemical state, had the highest percentage at the N100 location, suggesting that areas away from the steel works may have retained more of the original organic matter structure. C-N and C-O, as the second and third major chemical state, exhibited the highest percentage at the N20 position, possibly suggesting that soil SOM in areas close to steel works were subjected to more intense nitrogenation and oxidation processes (Chen et al., 2020). This distribution pattern may be related to the changes in soil physicochemical properties induced by ZVI contamination. Especially, the ZVI-induced changes in pH and ORP may have promoted the transformation of certain organic functional groups. COOH, as the least occupied chemical state in all samples, was

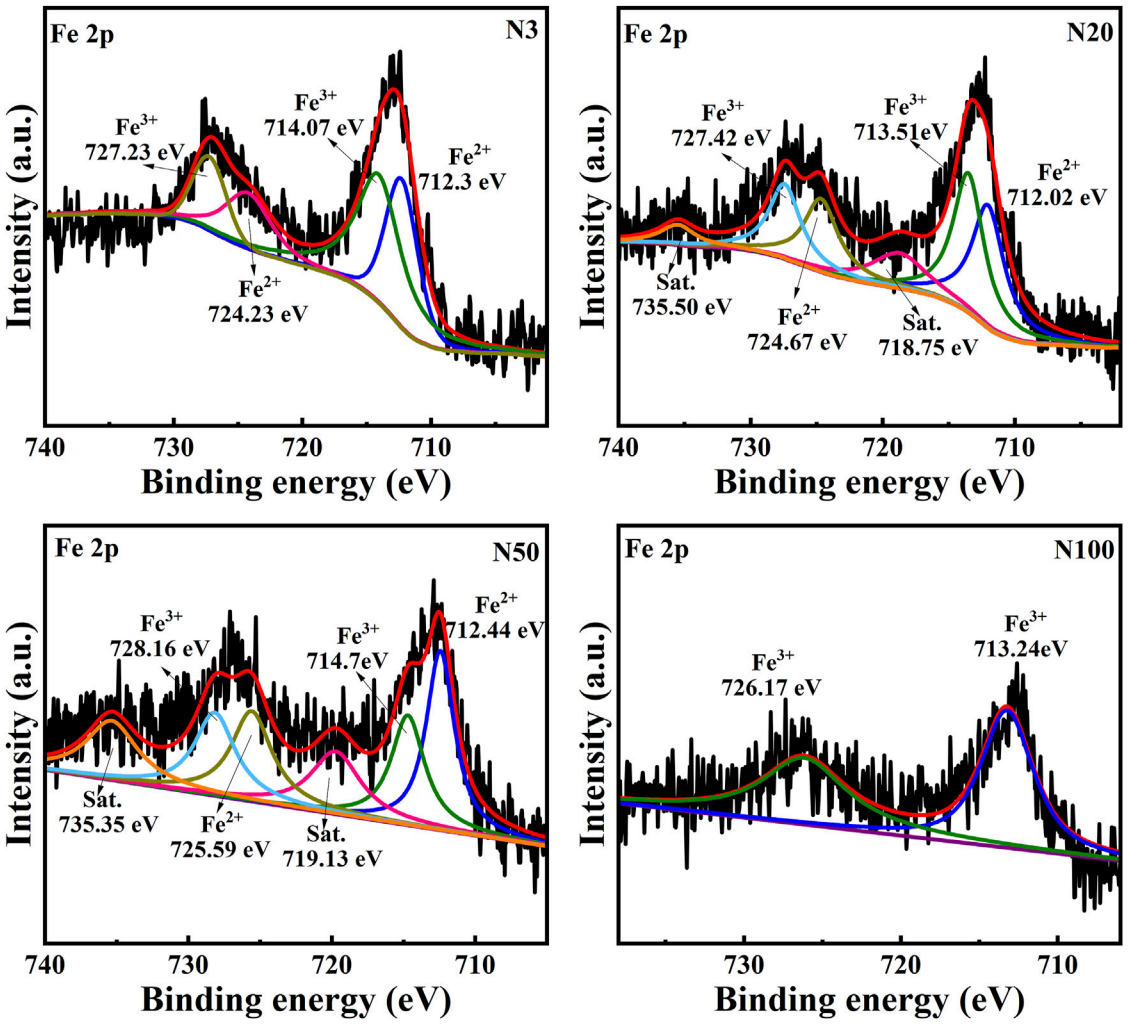

FIGURE 7
The XPS spectra of Fe 2p3/2 and Fe 2p1/2 with curve resolution into different components.

relatively high at N3 and N20 positions, which is in direct agreement with the findings of Yao et al. (2010). Carbon in biomass char can be oxidised to carbonyl after long-term pollution oxidation. Nano ZVI can generate ROS, which induces oxidative degradation of organic pollutants, such as drugs and herbicides (Phenrat et al., 2009; Machado et al., 2013; Karim et al., 2017). As a result, the oxidative degradation of organic matter is not only accelerated, but N_2O emissions from abiotic pathways may also be promoted. Bacterial residues were clearly visible in the N20 sampling zone in Figure 10. It can be inferred that the ZVI-based contamination caused the release of organic carbon sequestered in the core of microaggregates, which accelerated bacterial colonisation. Chen et al. (2020) found a significant interaction between organic functional groups on the surface of soil microaggregates and soil minerals.

FTIR analyses further supported these findings (Figure 9). The O-H stretching vibrations (bonded and non-bonded hydroxyl groups) were attributed to phenols, while alcohols exhibit variation in the wave number range 3,436–3,445 cm^{-1} (Gerzabek et al., 2006). The N3 position had the largest integral area, which decreased with increasing distance. This result indirectly confirms the larger content of hydroxyl radicals (HO-) at the N3 position, echoing the XPS results. Similarly, the peaks representing C=O vibrations in the range of 1,649–1,658 cm^{-1} showed a similar trend, further confirming a higher degree of organic matter oxidation at the near steel works location. It is also noteworthy that the peaks in the range 1,038–1,050 cm^{-1} represent the C-O stretching vibrations of polysaccharide or polysaccharide-like substances and the Si-O stretching vibrations. Its integration area was largest at the N3 position. This may reflect the impact of the ZVI-based pollution on soil microbial activities, leading to the accumulation of polysaccharides or altered soil mineralogy. Wang et al. (2020) showed that selective adsorption of ZVI may lead to significant changes in the properties of dissolved organic matter (DOM) including molecular size, composition and chemical properties. The lowest organic matter content was found in the soil at N3 location and the highest SOM content was found in the soil at N100. Besides, SOM increased with the increasing distance from the steel works (Table 3). This may be due to more intense ZVI-based contamination of soils in the near steel works domain, leading to

10.3389/fenvs.2024.1470746

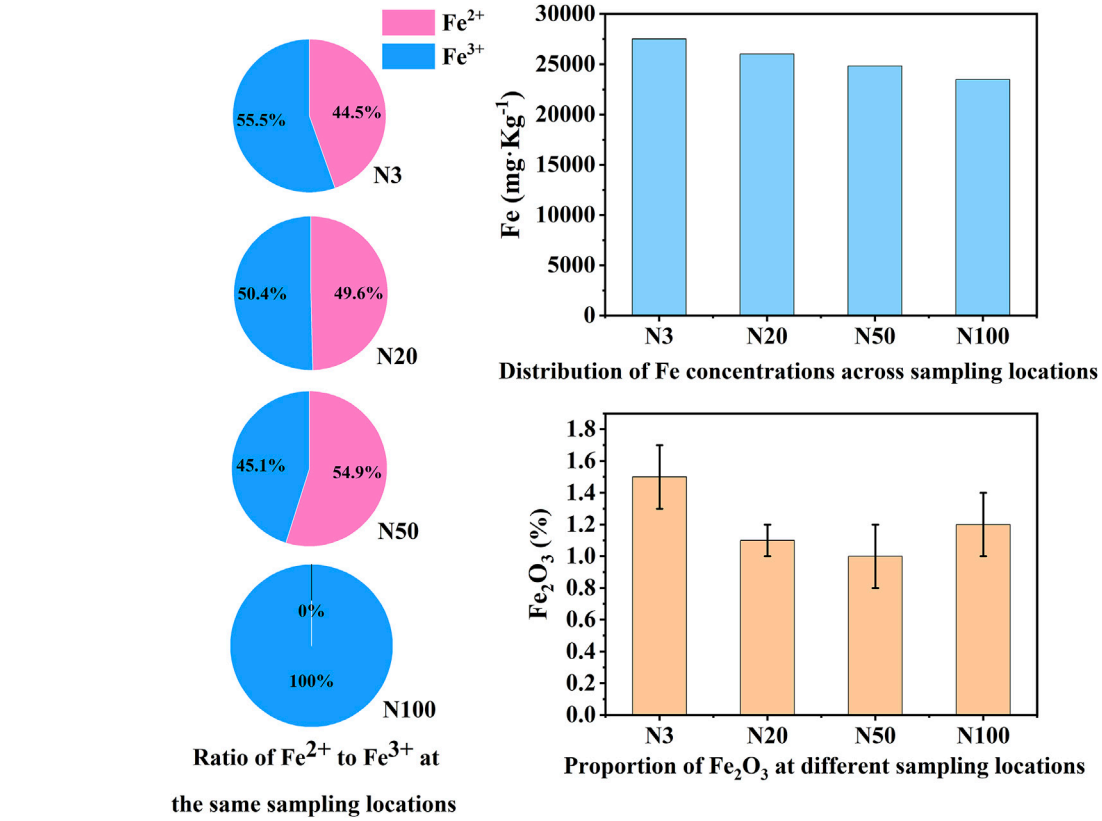

FIGURE 8
Iron speciation, concentration, and Fe_2O_3 distribution at N3, N20, N50, and N100 sampling locations.

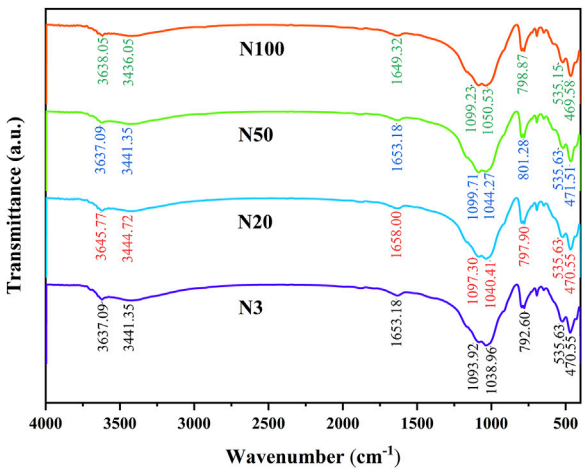

FIGURE 9
FTIR spectra at different sampling locations.

accelerated decomposition of organic matter (Vindedahl et al., 2016). Large amounts of ZVI may accelerate the decomposition of soil organic matter and affect soil carbon sequestration. Zhang et al. (2012) indicated that the semiconducting nature of iron oxide could accelerate the electron transfer process between the microorganisms and electron acceptors, which may promote the decomposition of organic matter by soil microorganisms. The work of Sun et al. (2019) further confirmed that Fe(III) reduction, as the main electron acceptor process, significantly promoted organic carbon decomposition.

TABLE 6 Integral of relative peak area of main peaks of FTIR spectrum.

λ/cm^{-1}	N3	N20	N50	N100
3,637–3,645	2.042 ± 0.111	1.909 ± 0.029	1.532 ± 0.055	1.408 ± 0.216
3,436–3,445	3.192 ± 0.137	2.462 ± 0.091	2.427 ± 0.126	2.239 ± 0.253
1,649–1,658	2.088 ± 0.094	1.925 ± 0.071	1.852 ± 0.045	1.651 ± 0.053
1,435–1,438	0.131 ± 0.164	0.033 ± 0.004	0.038 ± 0.004	0.022 ± 0.003
1,038–1,050	12.227 ± 0.666	11.886 ± 0.136	9.361 ± 0.261	10.283 ± 0.219
792–802	0.776 ± 0.033	0.912 ± 0.012	0.981 ± 0.034	0.945 ± 0.043
469–472	4.895 ± 0.069	5.352 ± 0.173	5.592 ± 0.202	5.435 ± 0.282

4.3 Dissipative structure of soil microaggregates and its impact due to the gradient ZVI-based pollution

From our analysis, it was found that the surface elemental composition and chemical state of soil microaggregates have

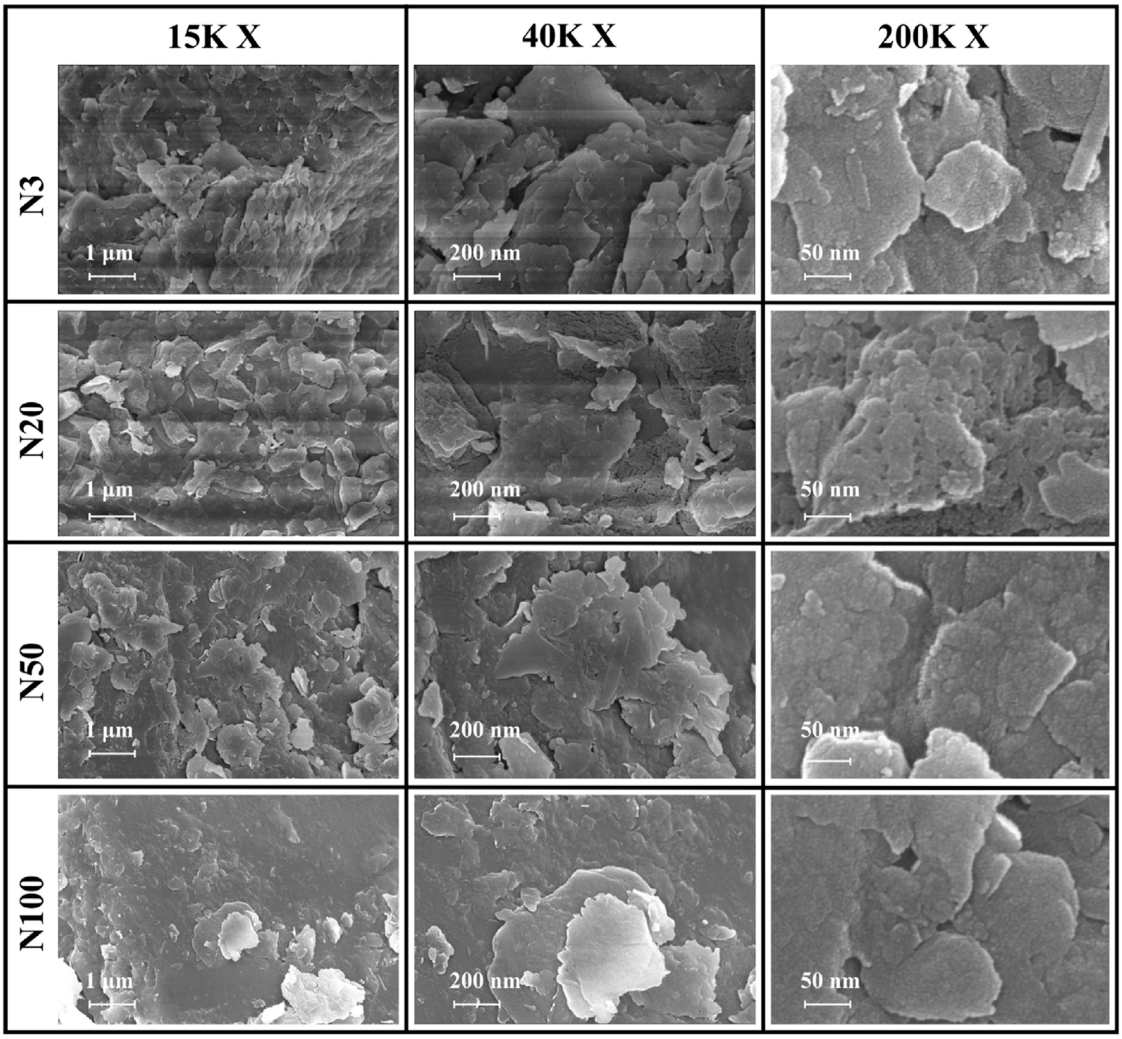

FIGURE 10
SEM images of soil aggregates at 15Kx, 40K x and 200Kx magnification of different sampling locations.

significant spatial differences, which were closely related to the ZVI-based pollution gradient in steel works. This spatial difference can be explained by considering the theory of dissipative structure. According to Prigotin's dissipative structure theory, an open system far from equilibrium can form a new ordered structure under certain conditions by continuously exchanging matter and energy with the environment. In this work, the material and energy flows introduced by the ZVI-based pollution drove the soil system away from its original equilibrium state. Near steel works (N3) samples exhibited the lowest pH, as well as the highest ORP and conductivity, suggesting that the ZVI-based contamination resulted in more acidified soil, altered the redox conditions, and increased salinity. This change in gradient can be seen as a response of the system to external perturbations, forming a new stabilising structure. The addition of ZVI may have triggered a series of self-organising processes, leading to the formation of positive feedback mechanisms. The decrease in pH may also have promoted the dissolution of iron, which in turn may have further accelerated the acidification process, forming an autocatalytic cycle. The impact of the ZVI-based pollution on the organic environment of soil microaggregates was particularly significant. The XPS and FTIR results showed that the near steel works sample N3 contained high levels of reactive oxygen radicals (ROS), especially hydroxyl radicals (HO-). This production of ROS can be regarded as a way for the system to dissipate excess substances. ROS not only accelerate the oxidative degradation of organic matter, but also may promote N_2O emission from abiotic pathways. These processes are important manifestations of the systematic dissipation of material and energy reorganisation. The gradient effect of the ZVI-based pollution was further confirmed by the valence distribution of Fe. The changes in the distribution of Fe (0), Fe(II), and Fe(III) from N3 to N100 reflect the spatial self-organisation of the system. This spatial self-organisation is a typical feature of dissipative structures. Changes in the Fe(II)/Fe(III) ratios directly affect the ORP of the soil, which in turn affects the chemical form and bioavailability of other elements in the microaggregates. This chain reaction demonstrates the interactions and synergistic effects among the components of the system, which is a key mechanism for the formation of dissipative structures. In general, changes in soil microaggregates due to ZVI pollution can be regarded as a

typical process of dissipative structure formation. The system forms new spatial structures and functional characteristics through self-organisation to adapt to changes in the external environment.

The dissipative structures due to the ZVI-based pollution not only affected soil physicochemical properties, but also significantly altered soil organic matter dynamics. The semiconducting nature of iron oxide may accelerate the electron transfer process between the microorganisms and electron acceptors (Zhang et al., 2012). This mechanism may have facilitated the accelerated decomposition of soil organic matter. Meanwhile, selective adsorption of ZVI may have altered the chemical stability and turnover rate of dissolved organic matter (DOM) (Wang et al., 2020), which in turn affected the carbon storage function of the soil. ZVI is often used for the remediation of pollution in organic environments (Sun et al., 2021). Nonetheless, excessive ZVI pollution may simultaneously lead to a reduction in soil organic carbon storage (Jones et al., 2012; Liu et al., 2021) and accelerate global climate change (Liu et al., 2019). These findings highlight the multifaceted effects of gradient ZVI-based pollution on soil ecosystems. However, this work still has some limitations. First, the focus was on the top soil layer and future studies should consider soil samples at different depths. Second, although the impact of the gradient ZVI-based pollution was observed on the organic environment and structure of soil microaggregates, further research is needed on the influence of these changes on soil functions, such as nutrient cycling and carbon storage in the long term. Future research could focus on the dynamics of dissipative structure formation and its long-term ecological effects.

5 Conclusion

This study thoroughly investigated the impact of gradient zero-valent iron (ZVI) pollution around steel works on soil microaggregates, revealing a series of complex physical, chemical, and biological processes. The results demonstrated that heavy metal contents, particularly Fe, significantly decreased with increasing distance from the steel works, indicating that industrial activities are the main source of these elements. Soil physicochemical properties showed obvious spatial variation patterns, with soils near the steel works being more acidified and strongly oxidized. The organic environment of soil microaggregates was significantly affected by the ZVI-based pollution gradient. High levels of reactive oxygen species (ROS) near the steel works accelerated the oxidative degradation of organic matter, leading to lower soil organic matter content. These changes may affect nutrient cycling and carbon storage, with implications for ecosystem services and climate change. The increased mobility of heavy metals in acidified and oxidized soils near steel works poses potential risks to human health through exposure pathways such as dust inhalation and consumption of contaminated food crops. The iron valence distribution exhibited spatial differences, with higher Fe^{2+} content near the steel works and Fe^{3+} dominating in areas farther away. This suggests an evolutionary sequence from Fe (0) oxidation to Fe(II) and then to Fe(III), highlighting the impact of ZVI contamination on iron cycling in soils.

Innovatively, the study identified the formation of dissipative structures in soil microaggregates due to ZVI pollution. These structures significantly affect soil physicochemical properties and the organic environment, providing a new perspective for understanding the impact of industrial pollutants on soil structure and function. Further research is recommended to investigate the long-term ecological effects of ZVI pollution on soil functions, such as nutrient cycling and carbon sequestration. Priority should be given to studying the mechanisms of dissipative structure formation in soil microaggregates and their influence on pollutant dynamics. Additionally, assessing the health risks associated with heavy metal exposure in local communities is essential for developing effective mitigation strategies. This study provides a scientific basis for soil protection, remediation, and environmental management strategies, contributing to the protection of soil ecosystem health in critical areas of the Earth.

Data availability statement

The raw data supporting the conclusions of this article will be made available by the authors, without undue reservation.

Author contributions

CL: Conceptualization, Data curation, Formal Analysis, Funding acquisition, Investigation, Methodology, Project administration, Software, Supervision, Validation, Visualization, Writing–original draft, Writing–review and editing. WX: Conceptualization, Writing–review and editing. SG: Funding acquisition, Writing–original draft. SS: Data curation, Methodology, Writing–review and editing. BL: Investigation, Writing–review and editing.

Funding

The author(s) declare that financial support was received for the research, authorship, and/or publication of this article. This work was supported by the Nanyang Normal University scientific research project [grant number ZX2015088], and the National Nature Science Foundation of China [grant number 41601614].

Conflict of interest

The authors declare that the research was conducted in the absence of any commercial or financial relationships that could be construed as a potential conflict of interest.

Publisher's note

References

Auffan, M., Achouak, W., Rose, J., Roncato, M. A., Chanéac, C., Waite, D. T., et al. (2008). Relation between the redox state of iron-based nanoparticles and their cytotoxicity toward *Escherichia coli*. *Environ. Sci. Technol.* 42 (17), 6730–6735. doi:10.1021/ES800086F

Bae, S., Collins, R. N., Waite, T. D., and Hanna, K. (2018). Advances in surface passivation of nanoscale zerovalent iron: a critical review. *Environ. Sci. Technol.* 52 (21), 12010–12025. doi:10.1021/ACS.EST.8B01734

Bae, S., and Hanna, K. (2015). Reactivity of nanoscale zero-valent iron in unbuffered systems: effect of pH and Fe(II) dissolution. *Environ. Sci. Technol.* 49 (17), 10536–10543. doi:10.1021/ACS.EST.5B01298

Bae, S., and Lee, W. (2010). Inhibition of nZVI reactivity by magnetite during the reductive degradation of 1,1,1-TCA in nZVI/magnetite suspension. *Appl. Catal. B Environ.* 96 (1-2), 10–17. doi:10.1016/J.APCATB.2010.01.028

Cerdà, A. (1996). Soil aggregate stability in three Mediterranean environments. *Soil Technol.* 9 (3), 133–140. doi:10.1016/S0933-3630(96)00008-6

Chen, H., Li, Q., Wang, M., Ji, D., and Tan, W. (2020). XPS and two-dimensional FTIR correlation analysis on the binding characteristics of humic acid onto kaolinite surface. *Sci. Total Environ.* 724, 138154. doi:10.1016/J.SCITOTENV.2020.138154

dos Santos, F. H., Soares, M. B., and Alleoni, L. R. F. (2022). Pristine and biochar-supported nano zero-valent iron to immobilize As, Zn and Pb in soil contaminated by smelting activities. *J. Environ. Manage.* 321, 116017. doi:10.1016/J.JENVMAN.2022.116017

Ersoy, O., Aydar, E., Gourgaud, A., and Bayhan, H. (2008). Quantitative analysis on volcanic ash surfaces: application of extended depth-of-field (focus) algorithm for light and scanning electron microscopy and 3D reconstruction. *Micron* 39 (2), 128–136. doi:10.1016/J.MICRON.2006.11.010

Gerzabek, M. H., Antil, R. S., Kögel-Knabner, I., Knicker, H., Kirchmann, H., and Haberhauer, G. (2006). How are soil use and management reflected by soil organic matter characteristics: a spectroscopic approach. *Eur. J. Soil Sci.* 57 (4), 485–494. doi:10.1111/J.1365-2389.2006.00794.X

He, D., Ma, J., Collins, R. N., and Waite, T. D. (2016). Effect of structural transformation of nanoparticulate zero-valent iron on generation of reactive oxygen species. *Environ. Sci. Technol.* 50 (7), 3820–3828. doi:10.1021/ACS.EST.5B04988

Hu, S., Lu, Y., Peng, L., Wang, P., Zhu, M., Dohnalkova, A. C., et al. (2018). Coupled kinetics of ferrihydrite transformation and As(v) sequestration under the effect of humic acids: a mechanistic and quantitative study. *Environ. Sci. Technol.* 52 (20), 11632–11641. doi:10.1021/ACS.EST.8B03492

Huang, X., Li, Y., Liu, B., Guggenberger, G., Shibistova, O., Zhu, Z., et al. (2017). SoilChip-XPS integrated technique to study formation of soil biogeochemical interfaces. *Soil Biol. biochem.* 113, 71–79. doi:10.1016/J.SOILBIO.2017.05.021

Jones, D. L., Rousk, J., Edwards-Jones, G., DeLuca, T. H., and Murphy, D. V. (2012). Biochar-mediated changes in soil quality and plant growth in a three year field trial. *Soil Biol. biochem.* 45, 113–124. doi:10.1016/J.SOILBIO.2011.10.012

Karim, S., Bae, S., Greenwood, D., Hanna, K., and Singhal, N. (2017). Degradation of 17α-ethinylestradiol by nano zero valent iron under different pH and dissolved oxygen levels. *Water Res.* 125, 32–41. doi:10.1016/J.WATRES.2017.08.029

Kelemen, S. R., Afeworki, M., Gorbaty, M. L., Kwiatek, P. J., Solum, M. S., Hu, J. Z., et al. (2002). XPS and ^{15}N NMR study of nitrogen forms in carbonaceous solids. *Energy fuels.* 16 (6), 1507–1515. doi:10.1021/ef0200828

Kögel-Knabner, I., Amelung, W., Cao, Z., Fiedler, S., Frenzel, P., Jahn, R., et al. (2010). Biogeochemistry of paddy soils. *Geoderma* 157 (1-2), 1–14. doi:10.1016/J.GEODERMA.2010.03.009

Kong, A. Y. Y., Scow, K. M., Córdova-Kreylos, A. L., Holmes, W. E., and Six, J. (2011). Microbial community composition and carbon cycling within soil microenvironments of conventional, low-input, and organic cropping systems. *Soil Biol. biochem.* 43 (1), 20–30. doi:10.1016/J.SOILBIO.2010.09.005

Krivoshein, P. K., Volkov, D. S., Rogova, O. B., and Proskurnin, M. A. (2022). FTIR photoacoustic and ATR spectroscopies of soils with aggregate size fractionation by dry sieving. *ACS Omega* 7 (2), 2177–2197. doi:10.1021/ACSOMEGA.1C05702

Kuzyakov, Y., and Blagodatskaya, E. (2015). Microbial hotspots and hot moments in soil: concept and review. *Soil Biol. biochem.* 83, 184–199. doi:10.1016/J.SOILBIO.2015.01.025

Lehmann, J., and Kleber, M. (2015). The contentious nature of soil organic matter. *Nature* 528 (7580), 60–68. doi:10.1038/NATURE16069

Li, C., and Guo, S. (2022). Structural evolution of soil aggregates in a karst rocky desertification area. *RSC Adv.* 12 (33), 21004–21013. doi:10.1039/D2RA02901D

Li, C., Guo, S., Shang, S., Qi, P., and Li, B. (2023). Structure and biogeochemical process of microaggregates in a water source area of China's south-to-north water diversion project according to different land use types. *Front. Environ. Sci.* 11, 1165454. doi:10.3389/FENVS.2023.1165454

Li, L., Zhang, L., Xia, J., Gippel, C. J., Wang, R., and Zeng, S. (2015). Implications of modelled climate and land cover changes on runoff in the middle route of the south to north water transfer project in China. *Water Resour. Manag.* 29 (8), 2563–2579. doi:10.1007/S11269-015-0957-3

Li, N., Han, L., Zhang, H., Huang, J., Luo, X., Li, X., et al. (2022). Polydopamine nanolayer assisted internal photo-deposition of CdS nanocrystals for stable cosensitized photoanode. *Nano Res.* 15 (10), 8836–8845. doi:10.1007/S12274-022-4588-8

Liu, M., Han, G., and Zhang, Q. (2019). Effects of soil aggregate stability on soil organic carbon and nitrogen under land use change in an erodible region in southwest China. *Int. J. Environ. Res. Public Health* 16 (20), 3809. doi:10.3390/IJERPH16203809

Liu, X., Wu, X., Liang, G., Zheng, F., Zhang, M., and Li, S. (2021). A global meta-analysis of the impacts of no-tillage on soil aggregation and aggregate-associated organic carbon. *L. Degrad. Dev.* 32 (18), 5292–5305. doi:10.1002/LDR.4109

Machado, S., Stawiński, W., Slonina, P., Pinto, A. R., Grosso, J. P., Nouws, H. P. A., et al. (2013). Application of green zero-valent iron nanoparticles to the remediation of soils contaminated with ibuprofen. *Sci. Total Environ.* 461-462, 323–329. doi:10.1016/J.SCITOTENV.2013.05.016

Marcon, L., Oliveras, J., and Puntes, V. F. (2021). *In situ* nanoremediation of soils and groundwaters from the nanoparticle's standpoint: a review. *Sci. Total Environ.* 791, 148324. doi:10.1016/J.SCITOTENV.2021.148324

Margenot, A. J., Calderón, F. J., Bowles, T. M., Parikh, S. J., and Jackson, L. E. (2015). Soil organic matter functional group composition in relation to organic carbon, nitrogen, and phosphorus fractions in organically managed tomato fields. *Soil Sci. Soc. Am. J.* 79 (3), 772–782. doi:10.2136/SSSAJ2015.02.0070

Melton, E. D., Swanner, E. D., Behrens, S., Schmidt, C., and Kappler, A. (2014). The interplay of microbially mediated and abiotic reactions in the biogeochemical Fe cycle. *Nat. Rev. Microbiol.* 12 (12), 797–808. doi:10.1038/NRMICRO3347

Nguyen, T. T., Janik, L. J., and Raupach, M. (1991). Diffuse reflectance infrared fourier transform (Drift) spectroscopy in soil studies. *Aust. J. Soil Res.* 29 (1), 49–67. doi:10.1071/SR9910049

Peltre, C., Bruun, S., Du, C., Thomsen, I. K., and Jensen, L. S. (2014). Assessing soil constituents and labile soil organic carbon by mid-infrared photoacoustic spectroscopy. *Soil Biol. biochem.* 77, 41–50. doi:10.1016/J.SOILBIO.2014.06.022

Phenrat, T., Long, T. C., Lowry, G. V., and Veronesi, B. (2009). Partial oxidation ("aging") and surface modification decrease the toxicity of nanosized zerovalent iron. *Environ. Sci. Technol.* 43 (1), 195–200. doi:10.1021/ES801955N

Soriano-Disla, J. M., Janik, L. J., Viscarra Rossel, R. A., MacDonald, L. M., and McLaughlin, M. J. (2014). The performance of visible, near-and mid-infrared reflectance spectroscopy for prediction of soil physical, chemical, and biological properties. *Appl. Spectrosc. Rev.* 49 (2), 139–186. doi:10.1080/05704928.2013.811081

Sun, K., He, W., Shen, Y., Yan, T., Liu, C., Yang, Z., et al. (2023). Ecological security evaluation and early warning in the water source area of the Middle Route of South-to-North Water Diversion Project. *Sci. Total Environ.* 868, 161561. doi:10.1016/J.SCITOTENV.2023.161561

Sun, X., Qin, Y., and Zhou, W. (2021). Degradation of amoxicillin from water by ultrasound-zero-valent iron activated sodium persulfate. *Sep. Purif. Technol.* 275, 119080. doi:10.1016/J.SEPPUR.2021.119080

Sun, Z., Qian, X., Shaaban, M., Wu, L., Hu, J., and Hu, R. (2019). Effects of iron(III) reduction on organic carbon decomposition in two paddy soils under flooding conditions. *Environ. Sci. Pollut. Res.* 26 (12), 12481–12490. doi:10.1007/S11356-019-04600-9

Vindedahl, A. M., Strehlau, J. H., Arnold, W. A., and Penn, R. L. (2016). Organic matter and iron oxide nanoparticles: aggregation, interactions, and reactivity. *Environ. Sci. Nano* 3 (3), 494–505. doi:10.1039/C5EN00215J

Wang, Y., Yang, K., and Lin, D. (2020). Nanoparticulate zero valent iron interaction with dissolved organic matter impacts iron transformation and organic carbon stability. *Environ. Sci. Nano* 7 (6), 1818–1830. doi:10.1039/D0EN00197J

Yamashita, T., and Hayes, P. (2008). Analysis of XPS spectra of Fe^{2+} and Fe^{3+} ions in oxide materials. *Appl. Surf. Sci.* 254 (8), 2441–2449. doi:10.1016/J.APSUSC.2007.09.063

Yao, F. X., Arbestain, M. C., Virgel, S., Blanco, F., Arostegui, J., Maciá-Agulló, J. A., et al. (2010). Simulated geochemical weathering of a mineral ash-rich biochar in a modified soxhlet reactor. *Chemosphere* 80 (7), 724–732. doi:10.1016/J.CHEMOSPHERE.2010.05.026

Zhang, G. Y., He, J. Z., Liu, F., and Zhang, L. M. (2014). Iron-manganese nodules harbor lower bacterial diversity and greater proportions of proteobacteria compared to bulk soils in four locations spanning from north to south China. *Geomicrobiol. J.* 31 (7), 562–577. doi:10.1080/01490451.2013.854428

Zhang, W., Li, X., Liu, T., and Li, F. (2012). Enhanced nitrate reduction and current generation by *Bacillus* sp. in the presence of iron oxides. *J. Soils Sediments* 12 (3), 354–365. doi:10.1007/S11368-011-0460-2

Zhou, T., Bo, X., Qu, J., Wang, L., Zhou, J., and Li, S. (2019). Characteristics of PCDD/Fs and metals in surface soil around an iron and steel plant in north China plain. *Chemosphere* 216, 413–418. doi:10.1016/J.CHEMOSPHERE.2018.10.024

Zhu, X., Yang, S., Wang, L., Liu, Y., Qian, F., Yao, W., et al. (2016). Tracking the conversion of nitrogen during pyrolysis of antibiotic mycelial fermentation residues using XPS and TG-FTIR-MS technology. *Environ. Pollut.* 211, 20–27. doi:10.1016/J.ENVPOL.2015.12.032